

# Hybrid 3D Printing of Soft Electronics

Alexander D. Valentine, Travis A. Busbee, John William Boley, Jordan R. Raney, Alex Chortos, Arda Kotikian, John Daniel Berrigan, Michael F. Durstock, and Jennifer A. Lewis\*

Hybrid 3D printing is a new method for producing soft electronics that combines direct ink writing of conductive and dielectric elastomeric materials with automated pick-and-place of surface mount electronic components within an integrated additive manufacturing platform. Using this approach, insulating matrix and conductive electrode inks are directly printed in specific layouts. Passive and active electrical components are then integrated to produce the desired electronic circuitry by using an empty nozzle (in vacuum-on mode) to pick up individual components, place them onto the substrate, and then deposit them (in vacuum-off mode) in the desired location. The components are then interconnected via printed conductive traces to yield soft electronic devices that may find potential application in wearable electronics, soft robotics, and biomedical devices.

The emerging field of soft electronics is driven by the growing interest in wearable electronics,<sup>[1–14]</sup> robotics,<sup>[15–17]</sup> and biomedical devices.<sup>[18,19]</sup> The two prevailing approaches to fabricating soft stretchable electronics employ conceptually different motifs. One approach uses high-performance electronic materials in unconventional geometries to achieve thin, bendable, and stretchable designs.<sup>[20,21]</sup> In this approach, conventional microfabrication methods are combined with approaches, such as transfer printing, to create stretchable battery arrays,<sup>[22]</sup> ultralightweight electronic foils,<sup>[23]</sup> solar cells,<sup>[24]</sup> and multiplexed biosensing electrode arrays.<sup>[25]</sup> The other approach is to fully print soft materials and components to create devices in stretchable motifs, utilizing conductive composites,<sup>[12,26–38]</sup> liquid metals,<sup>[39–41]</sup> and ionic liquids.<sup>[42–44]</sup>

Several printing methods have been introduced for electronic device fabrication due to their programmability, scalability, and low barrier-to-entry.<sup>[45–52]</sup> For example, inkjet printing enables

the fabrication of high-performance flexible transistors, although a combination of multistep subtractive and additive processes are required.<sup>[48,49]</sup> More recently, 3D electronics composed of flexible conductors and matrix materials have been fabricated by fused depositing modeling.<sup>[46,47]</sup> However, in these initial embodiments, several manual assembly steps were needed to achieve the desired device functionality. Finally, direct ink writing is a versatile approach, which has been used to create electrically small antennas,<sup>[50]</sup> soft sensors,<sup>[5,6,51]</sup> quantum dot light-emitting diodes (QD-LEDs),<sup>[52]</sup> and cardiac organ-on-chip devices with electronic readout.<sup>[53]</sup> However, to fully enable the program-

mable fabrication of high-performance soft electronics in arbitrary form factors for wearable applications, new printable conductive elastomers coupled with the integration of electronics manufacturing capabilities are needed.


Here, we report a new method, known as hybrid 3D printing, for producing soft electronics. Specifically, this method combines direct ink writing (DIW) with automated pick-and-place (P+P) of surface mount electronic components within a single manufacturing platform (**Figure 1**). Both insulating matrix (**Figure 1a**) and conductive electrode inks (**Figure 1b**) can be patterned in specific layouts, including soft sensing arrays (**Figure 1c**). Passive and active electrical components are then integrated to fabricate soft circuits by applying a modest vacuum through an empty nozzle to pick up individual components, place them onto the substrate, and then release the vacuum to deposit them in the desired location (**Figure 1d**; **Movie S1**, Supporting Information). Finally, conductive traces are printed to create electrical interconnects between the P+P components (**Figure 1e**). A representative motif is the flexible LED array shown in **Figure 1f**.

To create soft electronics via hybrid 3D printing, we first developed matrix and conductive inks based on a thermoplastic polyurethane (TPU) that is both biocompatible and highly stretchable. To produce the conductive electrode ink, we added silver flakes ( $\approx 2 \mu\text{m}$  lateral dimension) to the pure TPU ink. The AgTPU ink flows readily through fine nozzles due to its strong shear thinning behavior and retains its filamentary form upon exiting the nozzle due to its relatively high storage modulus ( $G' \approx 10^4 \text{ Pa}$ ) and shear yield stress ( $\tau_y \approx 20 \text{ Pa}$ ) (**Figure 2a–c**). Upon printing and drying, conductive electrodes with trace widths of  $100 \mu\text{m}$  or higher can be achieved that contain a percolating network of silver flakes

A. D. Valentine, T. A. Busbee, Dr. J. W. Boley, Dr. J. R. Raney,  
Dr. A. Chortos, A. Kotikian, Prof. J. A. Lewis  
Pierce Hall Rm 221

29 Oxford Street, Cambridge, MA 02138, USA  
E-mail: jalewis@seas.harvard.edu

Dr. J. D. Berrigan, Dr. M. F. Durstock  
Soft Materials Branch  
Materials and Manufacturing Directorate  
Air Force Research Laboratory  
Wright Patterson Air Force Base  
OH 45433, USA

 The ORCID identification number(s) for the author(s) of this article can be found under <https://doi.org/10.1002/adma.201703817>.

DOI: 10.1002/adma.201703817

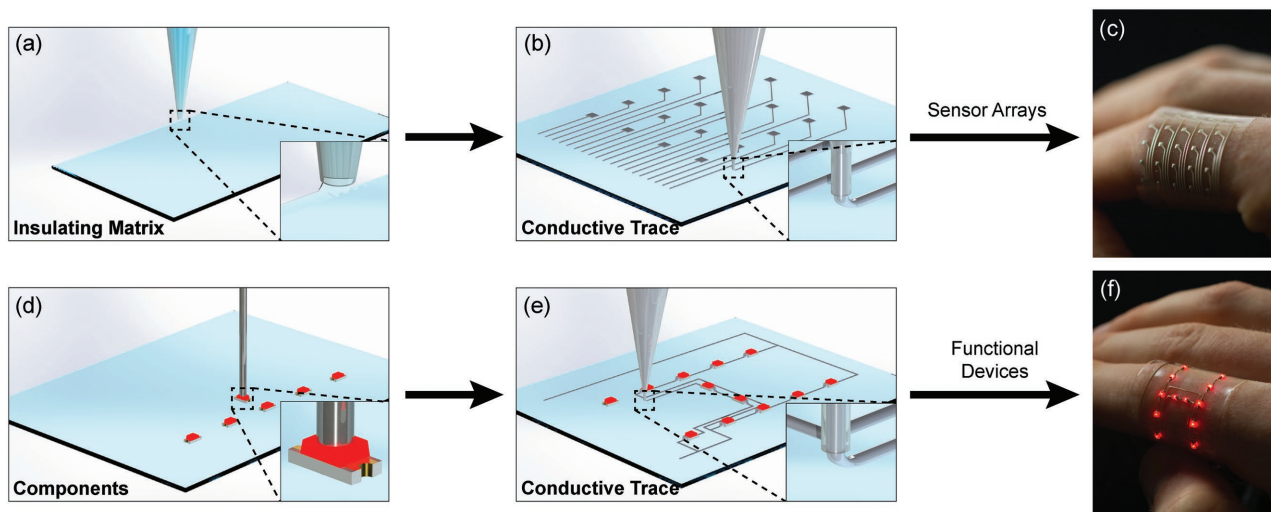


**Figure 1.** Hybrid 3D printing platform for soft electronics. Schematic images of a) direct ink writing of a TPU matrix for the device body and b) conductive AgTPU traces for the sensing elements. c) Image of representative example of soft sensor array. Schematic images of d) pick-and-place (P+P) of components using vacuum nozzle onto target positions and e) direct writing of conductive AgTPU traces to interconnect the surface mounted LEDs placed in the form of a soft, stretchable “H” LED array. f) Image of a functional LED array wrapped around a human finger.

(Figure 2d). By contrast, the pure TPU ink is a Newtonian fluid with a low apparent viscosity of  $\eta \approx 40$  Pa s that readily wets and spreads upon exiting the nozzle to form a cohesive

soft substrate (Figure 2c). Because they contain the same solvent, a robust interface develops between the AgTPU and pure TPU inks during printing (Figure S1, Supporting Information),

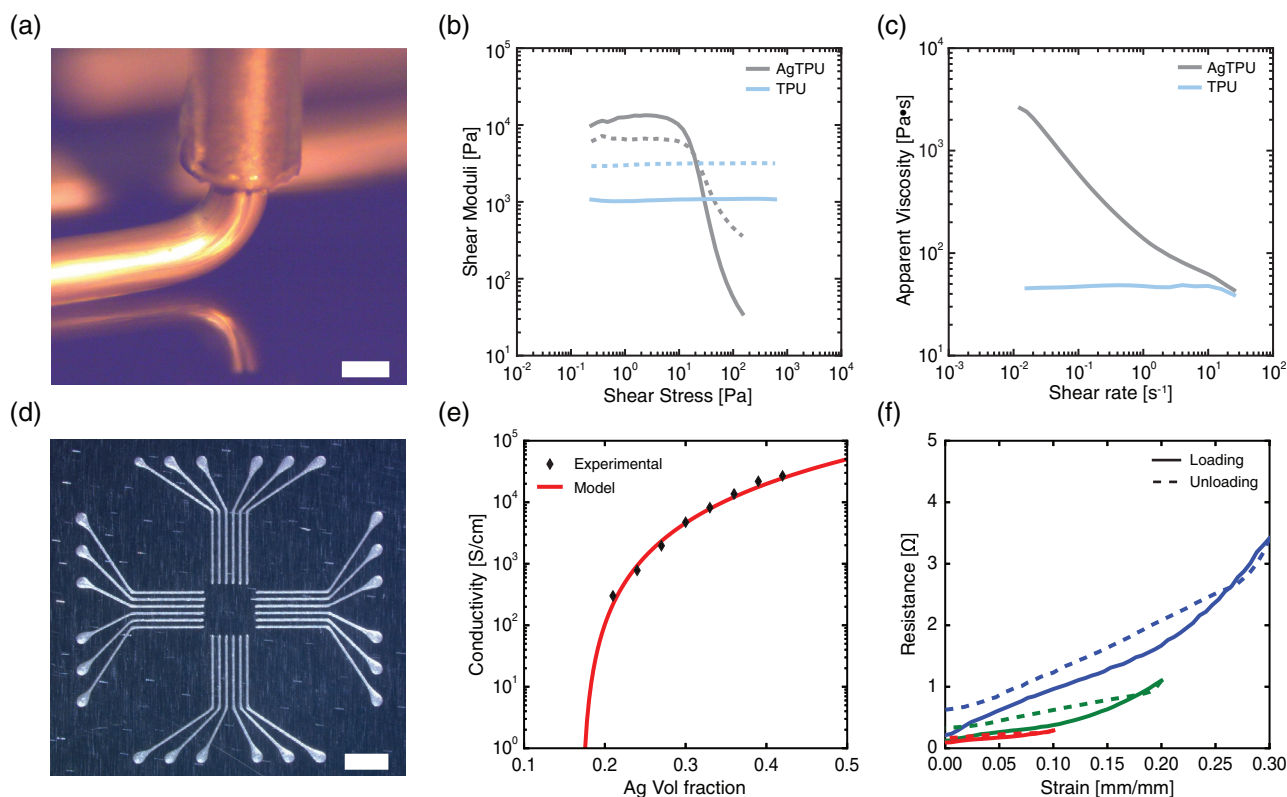


**Figure 2.** a) Image of direct writing of AgTPU ink through a 200  $\mu\text{m}$  nozzle (scale bar 200  $\mu\text{m}$ ). b) Shear moduli as a function of shear stress, comparing storage modulus  $G'$  (solid line) and loss modulus  $G''$  (dashed line) and c) apparent viscosity as a function of shear rate for the TPU and AgTPU inks. d) Direct writing of AgTPU electrodes in a 24-pad wiring scheme with electrode widths of 100  $\mu\text{m}$  (scale bar = 2 mm). e) Electrical conductivity of AgTPU composite as a function of silver flake content. Red line is a fit to the data (black) using the power-law relationship (from Equation (1)). f) Electrical resistance of AgTPU during single strain cycles of 10%, 20%, and 30% (red, green, and blue, respectively).

yielding soft electronic devices that do not exhibit delamination or cracking during or after stretching. This is a crucial feature of these inks, since delamination of printed electrodes from the underlying polymer matrix is a common mode of failure in soft electronics.<sup>[37,54]</sup>

The conductivity of AgTPU as a function of the volume fraction of silver flake is shown in Figure 2e, along with the respective power-law theory for a percolating network<sup>[55]</sup> given by

$$\sigma = \sigma_0 (V_f - V_c)^s \quad (1)$$

where  $\sigma$  is the conductivity of the AgTPU composite,  $\sigma_0$  is the bulk conductivity of silver,  $V_f$  is the volumetric fraction of silver flake (in dried form),  $V_c$  is the critical volume fraction at percolation (in dried form), and  $s$  is the power law exponent. Our experimental data are in good agreement with predicted behavior, yielding values of  $V_c = 0.171 \pm 0.01$  and  $s = 2.56 \pm 0.11$ . Due to their anisotropic nature, shear-induced alignment of silver flakes (Figure S2a, Supporting Information) within the AgTPU ink is expected during printing, which gives rise to a modest conductivity enhancement.<sup>[56,57]</sup> From these data, we chose to work with AgTPU inks composed of 36 vol% Ag, which exhibit an initial conductivity above  $10^4 \text{ S cm}^{-1}$ .

Using an electromechanical testing apparatus, we characterized the electrical properties of AgTPU in situ during mechanical stretching. AgTPU maintains an overall low resistance ( $<4 \text{ } \Omega$ ) through loading and unloading up to 30% strain

(Figure 2f). These distinctive unloading curves are likely a result of the well-known mechanical hysteresis of thermoplastic polyurethanes.<sup>[58]</sup> Further examination of an AgTPU specimen before and during stretching reveals permanent distortion of the silver flake-polymer network and stretching of the polymer matrix (Figure S2b,c, Supporting Information). When strained up to  $\approx 200\%$ , the electrical conductivity of the printed AgTPU electrodes decreases to a value of  $0.1 \text{ S cm}^{-1}$  (Figure S3, top, Supporting Information). At a higher strain of  $\approx 240\%$ , the electrodes undergo electrical failure due to a complete disruption of the percolative silver flake-polymer network. Triangular cyclic testing at 5% strain for 1000 cycles is used to investigate the electrical performance of the printed AgTPU features over extended stretching (Figure S3, bottom, Supporting Information). Given their high initial conductivity, low change in resistance, and long-term cyclic stability, our AgTPU inks yield mechanically robust, stretchable conductors.

To further investigate the performance of AgTPU, we fabricated the strain sensor shown in Figure 3a. Notably, the printed AgTPU electrodes exhibit a low electrical resistance coupled with a high normalized change in resistance ( $\Delta R/R_0$ ). When this device is subjected to a triangular strain cycle, it exhibits a linear, repeatable electrical response. A key figure of merit for evaluating strain sensor performance is the gauge factor ( $\text{GF} = (\Delta R/R_0)/\epsilon$ , where  $\Delta R/R_0$  denotes the relative resistance change and  $\epsilon$  denotes applied strain). By plotting these values, a GF of  $\approx 13.3$  is observed for the printed AgTPU electrodes,

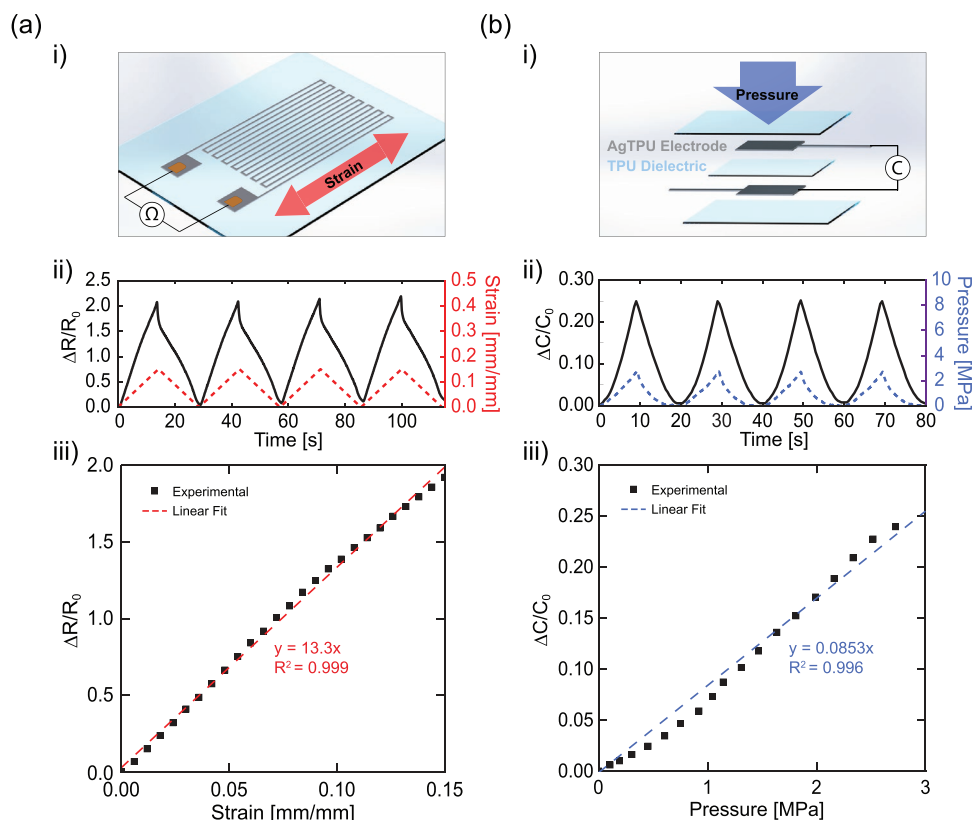


**Figure 3.** a) Strain sensor device and performance: i) device scheme, ii) plot of  $\Delta R/R_0$  over time during a triangular strain cycle, and iii) plot of  $\Delta R/R_0$  versus strain. b) Capacitive pressure sensor and performance: i) device scheme, ii) plot of  $\Delta C/C_0$  over time during a triangular strain cycle, and iii) plot of  $\Delta C/C_0$  versus pressure.

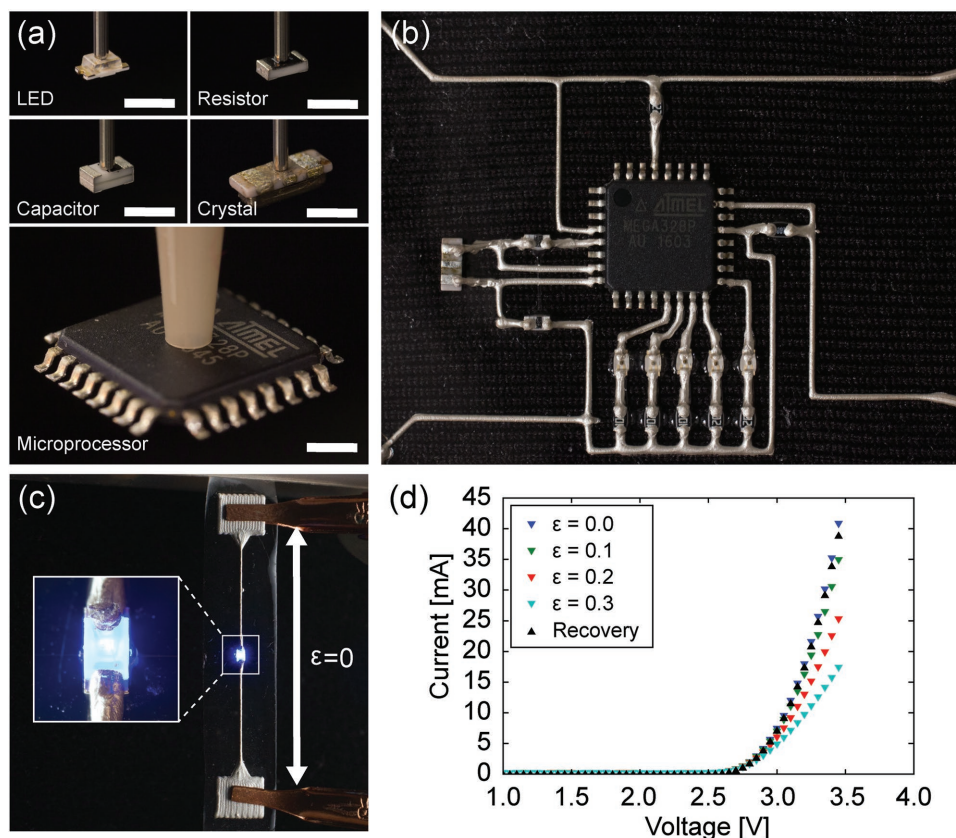


**Figure 4.** a) Images of pick-and-place of surface mount electrical components, including LED, resistor, capacitor, crystal oscillator, and microprocessor chip (scale bar = 2 mm). b) Image of microcontroller circuit fabricated by hybrid 3D printing, in which surface mount electrical components are interconnected with printed AgTPU electrodes onto an underlying TPU matrix. c) Image of hybrid 3D printed LED device; the inset shows interface of surface mount LED with the AgTPU electrodes. d) Current–voltage characteristics of LED device at 0%, 10%, 20%, 30% strains and upon releasing from strain (recovered state).

which is comparable to many other particle-laden composites used for strain sensors.<sup>[59–61]</sup>

Next, we printed a parallel-plate capacitive sensor composed of matrix and conductive materials in a multilayered architecture. The pure TPU matrix serves as an insulating layer with a dielectric constant of 9.1 and a low elastic modulus of  $E \approx 2.3$  MPa. The parallel-plate capacitive sensor uses the pure TPU as a deformable dielectric layer surrounded above and below by highly conductive AgTPU electrodes (Figure 3b). A cross-sectional view of the multilayer printed sensor is shown in Figure S4 in the Supporting Information. Upon applying an external pressure, the insulating layer thickness ( $d$ ) between the two printed electrodes is reduced, leading to a measurable increase in capacitance. Figure 3b shows the capacitive sensor response to multiple cycles of applied pressure, highlighting its consistent performance. In this device, the normalized change in capacitance,  $\Delta C/C_0$ , depends linearly on pressure (Figure 3b) up to 3 MPa.

To assess the accuracy of the automated P+P process, surface mount LEDs are placed from a cassette onto a grid for optical measurements (Figure S5a–c, Supporting Information). By comparing the target position to the actual position, we determined a positional error  $136 \mu\text{m} \pm 62$  ( $\approx 10\%$  of their overall dimensions) and rotational error of  $1.45^\circ \pm 1.05$  ( $n = 27$ ). This

method is reliable, allowing 52 components to be placed in a single step (Figure S5d and Movie S2, Supporting Information). **Figure 4a** illustrates P+P of five distinct components, with lateral dimensions ranging from  $0.8 \text{ mm} \times 1.6 \text{ mm}$  (LED) to  $9 \text{ mm} \times 9 \text{ mm}$  (microprocessor). By programming the target locations of 16 different components interconnected by printed electrodes in a customized layout, we can manufacture complex microcontroller devices, such as the representative device shown in Figure 4b.

These surface mount electrical components are composed of rigid materials that are orders of magnitude stiffer than the TPU printed matrix and AgTPU conductive electrodes. When these components are adhered to printed electrodes alone, delamination at the component-AgTPU interface occurs at very low strains ( $\epsilon = 0.14$ ). This observation arises due to poor bonding between the surface mount component and the printed AgTPU electrode. When stretched, stress concentration is localized at the component-electrode interface leading to delamination. To enhance bonding, small droplets of TPU are directly printed beneath each component body (Figure S6 and Movie S3, Supporting Information) to create an adhesive region that distributes the applied stress across the entire component-TPU matrix interface. This important modification led to nearly an order of magnitude higher strain to failure ( $\epsilon = 1.22$ ).



A representative device composed of 12 LEDs is now able to bend to a radius of curvature of 2.8 mm (Figure S7, Supporting Information) without experiencing any loss of functionality, i.e., significant reduction in LED intensity or mechanical failure.

Component integration is further characterized by fabricating a model architecture using our hybrid 3D printing method (Figure 4c). Specifically, we print an insulating matrix (TPU), P+P an LED component, and then print conductive interconnects (AgTPU). Current–voltage responses of this model device are acquired at various strains. The resulting current decreases with different values of strain ( $\epsilon = 0.3$ ). However, the current–voltage characteristics seem to completely recover after the specimen is returned to its original length (Figure 4d), which further illustrates our ability to reliably incorporate conventional electrical components into soft, stretchable devices in a robust manner.

To fully demonstrate our hybrid 3D printing platform, we created a complex microcontroller device coupled with a strain sensor and a large-area soft sensor array. The wearable electronic system is fabricated by co-printing both the TPU matrix and AgTPU electrodes along with P+P of a microcontroller chip and LEDs (Figure 5a; Movie S3, Supporting Information). The printed strain sensor is positioned posterior to the elbow joint and serves to provide strain data input to the microcontroller that corresponds to various joint angles. The microcontroller

circuit is designed using an ATMEGA328 chip (Atmel) to read the sensor data and output the readout to five indicator LEDs (Figure S8, Supporting Information). A custom-programmed script is loaded onto the chip prior to assembly, which can be further modified to carry out other functions. This textile-mounted soft electronic system functions in real time (Movie S4, Supporting Information), providing the user with visual feedback corresponding to the extent of joint bending (Figure 5b,c).

As a final embodiment, we created a sensor array composed of 29 capacitive sensors in the custom shape of a person's left foot (Figure 5d). Device fabrication is shown in Movie S5 in the Supporting Information. A carbon black-doped TPU (see the Experimental Section) is used as the insulating matrix (bottom layers) to enhance the visualization of the printed AgTPU electrodes. This plantar sensor array is designed with a multiplexed wire scheme to minimize the number of external connections. Using this layout, only 19 connections are needed rather than 58 (i.e., 2 electrodes for each of the 29 sensors). In the absence of applied pressure (Figure 5e) the sensors do not experience any deformation and, hence, no change in capacitance. During walking, the sensor array is deformed (Figure 5f) and the relative capacitance of each sensor is measured, resulting in a unique plantar pressure profile (all sensors are calibrated previous to testing). Given the soft, flexible form factor of the

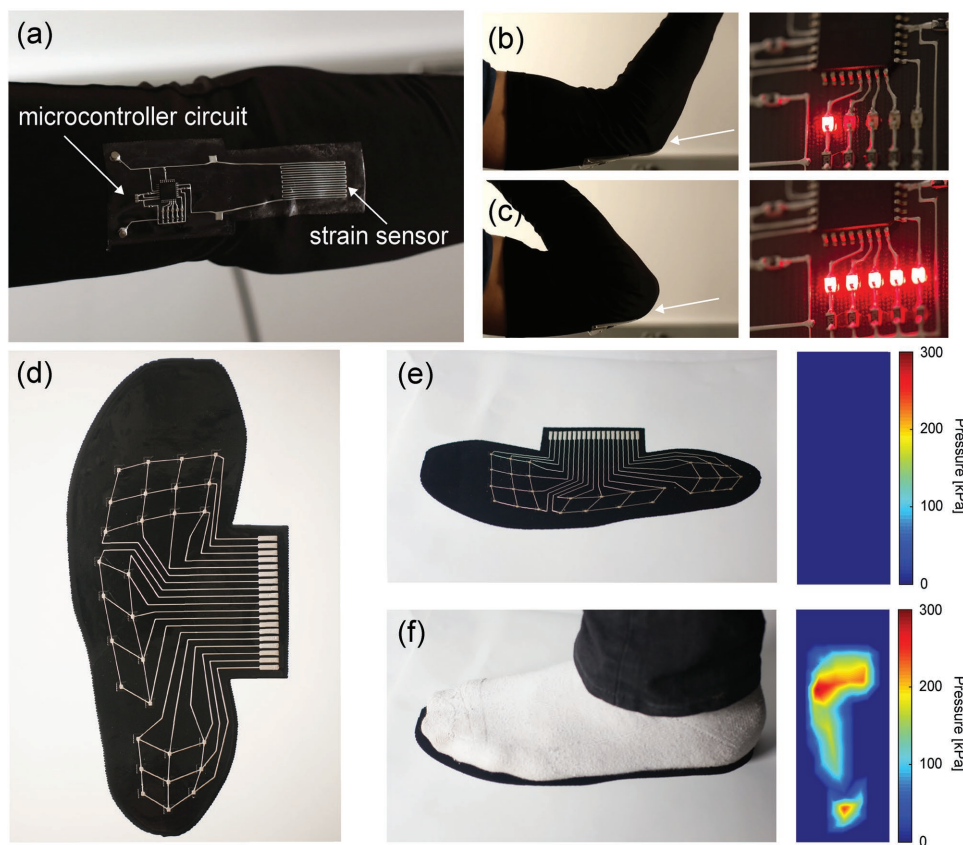


**Figure 5.** Wearable soft electronics fabricated by hybrid 3D printing: a) image of textile-mounted printed strain sensor and microcontroller circuit. b,c) Images of real-time function of the wearable strain device (identified with arrows) at modest and maximum joint bending, respectively, along with the corresponding LED readout. d) Image of plantar sensor array. e) Illustration of sensor array readout in the absence of applied pressure and f) upon the application of pressure by a human foot.

plantar sensor array, it could readily be integrated into the insole of a shoe and used to read out pressure profiles.

In summary, we report a new hybrid method for manufacturing high-performance soft electronics that combines direct ink writing with automated pick-and-place of surface mount electrical components. By developing novel insulating and conductive inks, functional strain and pressure sensors were fabricated and characterized. This hybrid method enables surface mount electrical components of arbitrary shapes and sizes to be readily integrated onto printed soft wearable circuits. Importantly, the broad set of printable materials (e.g., ceramics, polymers, metals) and devices (e.g., antennas, batteries, waveguides) previously developed for DIW offers an unique opportunity to expand the functionality 3D printed structures via this hybrid manufacturing platform.

## Experimental Section

**Materials System:** The insulating ink was prepared by dissolving TPU (Elastollan Soft 35A) in a cosolvent system composed of *N,N*-dimethylformamide (DMF) and tetrahydrofuran (THF) (Sigma-Aldrich) at 1:4 DMF:THF ratio by volume (v/v). The conductive ink was prepared by first dissolving TPU (Elastollan Soft 35A) in *N,N*-dimethylformamide and then adding silver flake, 99.95%, APS 2–5 μm (Inframat Advanced Materials), followed by mixing in a planetary mixer (FlackTek Speedmixer) for 30 min total in 10 min increments, waiting 10 min between mixing steps. Both pure TPU (matrix) and AgTPU (conductive) inks were loaded into 3 cc syringes, centrifuged at 3000 rpm for 2 min to remove air bubbles, and prepared for direct ink writing.

**Rheology Measurements:** The rheological properties of both TPU and AgTPU inks were characterized under ambient conditions using a controlled stress rheometer (AR 2000ex, TA Instruments) equipped with a 40 mm tapered cone plate geometry (2.005°, 56 μm truncation gap). The conductive ink was mixed using a FlackTek Speedmixer for 5 min at 2350 rpm prior to rheological characterization. A solvent trap was used to limit evaporation during these measurements. Viscometry measurements were carried out over shear rates from 0.001 to 100 s<sup>-1</sup>, while oscillatory measurements were carried out at a frequency of 1 Hz within the stress range of 0.01–10 000 Pa.

**Hybrid 3D Printing:** Printing was carried out with a three-axis motion-controlled stage (Aerotech) equipped with four independent z-axes that enable up to four inks to be coprinted. Print paths were generated with custom, open-source Python libraries (MeCode). Pneumatic-driven extrusion of inks was controlled with a digital pneumatic regulator (Ultimus V High Precision Dispenser, EFD) using 410 and 200 μm tapered dispense tips (EFD) for insulating TPU matrix and conductive AgTPU inks, respectively. Individual layers were cured at 80 °C for 2 h. Automated pick-and-place of different surface mount electrical components was carried out by mounting an empty syringe on one of the z-axes coupled with use of the vacuum function on a digital pneumatic regulator (Ultimus V High Precision Dispenser, EFD). The empty syringe along with its 250 μm metal capillary nozzle (EFD) was translated directly above a given component sitting in its stock cavity. Once the nozzle comes into contact with the component, the vacuum function is activated. The component was then translated to its target position and lowered, where the vacuum was removed to allow the component to be placed onto the soft substrate.

**Conductivity Measurements:** AgTPU samples were printed into thin rectangular films (2 cm × 0.3 cm). After curing at 80 °C for 2 h, sample thicknesses were measured using a stylus profilometer. Electrical resistance measurements were acquired using a four-point resistance probe (RM3544, Hioki). The Levenberg–Marquardt method was used to obtain a power-law fit.

**Electromechanical Characterization:** Printed AgTPU samples were attached to a uniaxial tensile testing setup (Model 5566, Instron)

and connected to a four-point resistance probe (RM3544, Hioki) for combined electromechanical testing. Multistrain tensile testing were conducted at 0.3 mm s<sup>-1</sup> and fixed-strain cyclic tensile testing at 1.0 mm s<sup>-1</sup>.

**Capacitive Pressure Sensor Measurement:** Printed sensor loads were applied and measured using a rigid acrylic fixture mounted to a compression testing apparatus (Model 5566, Instron). Capacitances were measured using an LCR (inductance, capacitance, resistance) meter (Model 880, B&K Precision).

**Model LED Device Characterization:** Specimens were subjected to a uniaxial strain in a tensile testing setup (Model 5566, Instron), while their current–voltage (*I*–*V*) response was measured using a source meter (Keithley 2400). A custom Matlab script was used to collect *I*–*V* response of an LED (LED Super Red 0603, LITE-ON) during strain testing.

**Plantar Sensor Array:** The TPU substrate ink was prepared identically to the insulating matrix ink with the addition of 2 wt% carbon black (Vulcan XC72R, Cabot) to aid in visualization. Capacitive pressure sensors were fabricated by printing alternating layers of AgTPU and TPU on the substrate. The bottom AgTPU electrode (≈40 μm thick) was printed first, followed by the dielectric TPU (≈160 μm thick), and, finally, the top AgTPU electrode (≈40 μm thick). Each capacitive element was then coated with a printed TPU layer (≈150 μm thick) and cured at 80 °C for 2 h. A soft silicone piece with rigid acrylic inclusions was used as an intermediate layer between the foot and the array to concentrate pressure on each capacitive sensor. After each individual sensor was calibrated, the pressure data was calculated using the total area associated with the sensor array, including space between sensors.

**Microcontroller Design and Components:** A microcontroller device was fabricated via hybrid 3D printing using surface mount LEDs (LED Super Red 0603, LITE-ON), resistors (SMD 0603, Vishay), capacitors (SMD 0603, AVX), a crystal oscillator (SMD 3-pin, Murata), and a microcontroller chip (ATmega328P, Atmel). The chip was programmed using a custom Arduino script.

## Supporting Information

Supporting Information is available from the Wiley Online Library or from the author.

## Acknowledgements

The authors gratefully acknowledge support provided from the Air Force Research Laboratory, Materials and Manufacturing Directorate and UES, Inc. (S-875-040-017) and support from the Vannevar Bush Faculty Fellowship Program sponsored by the Basic Research Office of the Assistant Secretary of Defense for Research and Engineering and funded by the Office of Naval Research Grant N00014-16-1-2823. The authors thank J. Muth, R. Truby, D. Kolesky, S. Gladman, J. Ahrens, L. Sanders, and J. Hardin for technical assistance and useful discussions. Finally, JAL thanks the GETTYLAB for their generous donation in support of our research.

## Conflict of Interest

Jennifer Lewis is a co-founder of Voxel8, Inc, which focuses on multi material, 3D printing.

## Keywords

conductive elastomers, multimaterial 3D printing, pick-and-place, soft sensors

Received: July 9, 2017

Revised: August 3, 2017

Published online:

- [1] S. Xu, Y. Zhang, L. Jia, K. E. Mathewson, K.-I. Jang, J. Kim, H. Fu, X. Huang, P. Chava, R. Wang, S. Bhole, L. Wang, Y. J. Na, Y. Guan, M. Flavin, Z. Han, Y. Huang, J. A. Rogers, *Science* **2014**, *344*, 70.
- [2] T. Yamada, Y. Hayamizu, Y. Yamamoto, Y. Yomogida, A. Izadi-Najafabadi, D. N. Futaba, K. Hata, *Nat. Nanotechnol.* **2011**, *6*, 296.
- [3] C. Pang, G.-Y. Lee, T. Kim, S. M. Kim, H. N. Kim, S.-H. Ahn, K.-Y. Suh, *Nat. Mater.* **2012**, *11*, 795.
- [4] C. H. Lee, Y. Ma, K.-I. Jang, A. Banks, T. Pan, X. Feng, J. S. Kim, D. Kang, M. S. Raj, B. L. McGrane, B. Morey, X. Wang, R. Ghaffari, Y. Huang, J. A. Rogers, *Adv. Funct. Mater.* **2015**, *25*, 3698.
- [5] A. Frutiger, J. T. Muth, D. M. Vogt, Y. Mengüç, A. Campo, A. D. Valentine, C. J. Walsh, J. A. Lewis, *Adv. Mater.* **2015**, *27*, 2440.
- [6] J. T. Muth, D. M. Vogt, R. L. Truby, Y. Mengüç, D. B. Kolesky, R. J. Wood, J. A. Lewis, *Adv. Mater.* **2014**, *26*, 6307.
- [7] W. Gao, S. Emaminejad, H. Y. Y. Nyein, S. Challa, K. Chen, A. Peck, H. M. Fahad, H. Ota, H. Shiraki, D. Kiriya, D.-H. Lien, G. A. Brooks, R. W. Davis, A. Javey, *Nature* **2016**, *529*, 509.
- [8] J. A. Rogers, Z. Bao, K. Baldwin, A. Dodabalapur, B. Crone, V. R. Raju, V. Kuck, H. Katz, K. Amundson, J. Ewing, P. Drzaic, *Proc. Natl. Acad. Sci. USA* **2001**, *98*, 4835.
- [9] T. Someya, T. Sekitani, S. Iba, Y. Kato, H. Kawaguchi, T. Sakurai, *Proc. Natl. Acad. Sci. USA* **2004**, *101*, 9966.
- [10] T. Someya, Y. Kato, T. Sekitani, S. Iba, Y. Noguchi, Y. Murase, H. Kawaguchi, T. Sakurai, *Proc. Natl. Acad. Sci. USA* **2005**, *102*, 12321.
- [11] K. Takei, T. Takahashi, J. C. Ho, H. Ko, A. G. Gillies, P. W. Leu, R. S. Fearing, A. Javey, *Nat. Mater.* **2010**, *9*, 821.
- [12] D. J. Lipomi, M. Vosgueritchian, B. C.-K. Tee, S. L. Hellstrom, J. A. Lee, C. H. Fox, Z. Bao, *Nat. Nanotechnol.* **2011**, *6*, 788.
- [13] D.-H. Kim, N. Lu, R. Ma, Y.-S. Kim, R.-H. Kim, S. Wang, J. Wu, S. M. Won, H. Tao, A. Islam, K. J. Yu, T. Kim, R. Chowdhury, M. Ying, L. Xu, M. Li, H.-J. Chung, H. Keum, M. McCormick, P. Liu, Y.-W. Zhang, F. G. Omenetto, Y. Huang, T. Coleman, J. A. Rogers, *Science* **2011**, *333*, 838.
- [14] J. Kim, M. Lee, H. J. Shim, R. Ghaffari, H. R. Cho, D. Son, Y. H. Jung, M. Soh, C. Choi, S. Jung, K. Chu, D. Jeon, S.-T. Lee, J. H. Kim, S. H. Choi, T. Hyeon, D.-H. Kim, *Nat. Commun.* **2014**, *5*, 5747.
- [15] R. V. Martinez, J. L. Branch, C. R. Fish, L. Jin, R. F. Shepherd, R. M. D. Nunes, Z. Suo, G. M. Whitesides, *Adv. Mater.* **2013**, *25*, 205.
- [16] M. Wehner, R. L. Truby, D. J. Fitzgerald, B. Mosadegh, G. M. Whitesides, J. A. Lewis, R. J. Wood, *Nature* **2016**, *536*, 451.
- [17] A. D. Marchese, C. D. Onal, D. Rus, *Soft Rob.* **2014**, *1*, 75.
- [18] H. C. Ko, M. P. Stoykovich, J. Song, V. Malyarchuk, W. M. Choi, C.-J. Yu, J. B. Geddes Iii, J. Xiao, S. Wang, Y. Huang, J. A. Rogers, *Nature* **2008**, *454*, 748.
- [19] O. Graudejus, B. Morrison, C. Goletiani, Z. Yu, S. Wagner, *Adv. Funct. Mater.* **2012**, *22*, 640.
- [20] D.-Y. Khang, H. Jiang, Y. Huang, J. A. Rogers, *Science* **2006**, *311*, 208.
- [21] D.-H. Kim, J. Xiao, J. Song, Y. Huang, J. A. Rogers, *Adv. Mater.* **2010**, *22*, 2108.
- [22] S. Xu, Y. Zhang, J. Cho, J. Lee, X. Huang, L. Jia, J. A. Fan, Y. Su, J. Su, H. Zhang, H. Cheng, B. Lu, C. Yu, C. Chuang, T. Kim, T. Song, K. Shigeta, S. Kang, C. Dagdeviren, I. Petrov, P. V. Braun, Y. Huang, U. Paik, J. A. Rogers, *Nat. Commun.* **2013**, *4*, 1543.
- [23] M. Kaltenbrunner, T. Sekitani, J. Reeder, T. Yokota, K. Kuribara, T. Tokuhara, M. Drack, R. Schwödiauer, I. Graz, S. Bauer-Gogonea, S. Bauer, T. Someya, *Nature* **2013**, *499*, 458.
- [24] D. J. Lipomi, B. C.-K. Tee, M. Vosgueritchian, Z. Bao, *Adv. Mater.* **2011**, *23*, 1771.
- [25] J. Viventi, D.-H. Kim, L. Vigeland, E. S. Frechette, J. A. Blanco, Y.-S. Kim, A. E. Avrin, V. R. Tiruvadi, S.-W. Hwang, A. C. Vanleer, D. F. Wulsin, K. Davis, C. E. Gelber, L. Palmer, J. van der Spiegel, J. Wu, J. Xiao, Y. Huang, D. Contreras, J. A. Rogers, B. Litt, *Nat. Neurosci.* **2011**, *14*, 1599.
- [26] T. Sekitani, Y. Noguchi, K. Hata, T. Fukushima, T. Aida, T. Someya, *Science* **2008**, *321*, 1468.
- [27] T. Sekitani, H. Nakajima, H. Maeda, T. Fukushima, T. Aida, K. Hata, T. Someya, *Nat. Mater.* **2009**, *8*, 494.
- [28] K.-Y. Chun, Y. Oh, J. Rho, J.-H. Ahn, Y.-J. Kim, H. R. Choi, S. Baik, *Nat. Nanotechnol.* **2010**, *5*, 853.
- [29] D. Wang, H. Li, M. Li, H. Jiang, M. Xia, Z. Zhou, *J. Mater. Chem. C* **2013**, *1*, 2744.
- [30] Z. Wang, Y. Huang, J. Sun, Y. Huang, H. Hu, R. Jiang, W. Gai, G. Li, C. Zhi, *ACS Appl. Mater. Interfaces* **2016**, *8*, 24837.
- [31] S. Yun, X. Niu, Z. Yu, W. Hu, P. Brochu, Q. Pei, *Adv. Mater.* **2012**, *24*, 1321.
- [32] W. Hu, X. Niu, L. Li, S. Yun, Z. Yu, Q. Pei, *Nanotechnology* **2012**, *23*, 344002.
- [33] Y. Tang, S. Gong, Y. Chen, L. W. Yap, W. Cheng, *ACS Nano* **2014**, *8*, 5707.
- [34] T. Chen, Y. Xue, A. K. Roy, L. Dai, *ACS Nano* **2014**, *8*, 1039.
- [35] Z. Chen, W. Ren, L. Gao, B. Liu, S. Pei, H.-M. Cheng, *Nat. Mater.* **2011**, *10*, 424.
- [36] M. Park, J. Im, M. Shin, Y. Min, J. Park, H. Cho, S. Park, M.-B. Shim, S. Jeon, D.-Y. Chung, J. Bae, J. Park, U. Jeong, K. Kim, *Nat. Nanotechnol.* **2012**, *7*, 803.
- [37] N. Matsuhisa, M. Kaltenbrunner, T. Yokota, H. Jinno, K. Kuribara, T. Sekitani, T. Someya, *Nat. Commun.* **2015**, *6*, 7461.
- [38] Y. Kim, J. Zhu, B. Yeom, M. Di Prima, X. Su, J.-G. Kim, S. J. Yoo, C. Uher, N. A. Kotov, *Nature* **2013**, *500*, 59.
- [39] Y.-L. Park, B.-R. Chen, R. J. Wood, *IEEE Sens. J.* **2012**, *12*, 2711.
- [40] H.-J. Koo, J.-H. So, M. D. Dickey, O. D. Velev, *Adv. Mater.* **2011**, *23*, 3559.
- [41] J.-H. So, J. Thelen, A. Qusba, G. J. Hayes, G. Lazzi, M. D. Dickey, *Adv. Funct. Mater.* **2009**, *19*, 3632.
- [42] H. Ota, K. Chen, Y. Lin, D. Kiriya, H. Shiraki, Z. Yu, T.-J. Ha, A. Javey, *Nat. Commun.* **2014**, *5*, 5032.
- [43] B. Chen, J. J. Lu, C. H. Yang, J. H. Yang, J. Zhou, Y. M. Chen, Z. Suo, *ACS Appl. Mater. Interfaces* **2014**, *6*, 7840.
- [44] J. L. Bideau, L. Viau, A. Vioux, *Chem. Soc. Rev.* **2011**, *40*, 907.
- [45] E. MacDonald, R. Wicker, *Science* **2016**, *353*, aaf2093.
- [46] H. Ota, S. Emaminejad, Y. Gao, A. Zhao, E. Wu, S. Challa, K. Chen, H. M. Fahad, A. K. J. ha, D. Kiriya, W. Gao, H. Shiraki, K. Morioka, A. R. Ferguson, K. E. Healy, R. W. Davis, A. Javey, *Adv. Mater. Technol.* **2016**, *1*, 1600013.
- [47] D. Zhang, B. Chi, B. Li, Z. Gao, Y. Du, J. Guo, J. Wei, *Synth. Met.* **2016**, *217*, 79.
- [48] A. C. Arias, S. E. Ready, R. Lujan, W. S. Wong, K. E. Paul, A. Salleo, M. L. Chabinyc, R. Apte, R. A. Street, Y. Wu, P. Liu, B. Ong, *Appl. Phys. Lett.* **2004**, *85*, 3304.
- [49] A. Pierre, M. Sadeghi, M. M. Payne, A. Facchetti, J. E. Anthony, A. C. Arias, *Adv. Mater.* **2014**, *26*, 5722.
- [50] J. J. Adams, E. B. Duoss, T. F. Malkowski, M. J. Motala, B. Y. Ahn, R. G. Nuzzo, J. T. Bernhard, J. A. Lewis, *Adv. Mater.* **2011**, *23*, 1335.
- [51] S.-Z. Guo, K. Qiu, F. Meng, S. H. Park, M. C. McAlpine, *Adv. Mater.* **2017**, *29*, 1701218.
- [52] Y. L. Kong, I. A. Tamargo, H. Kim, B. N. Johnson, M. K. Gupta, T.-W. Koh, H.-A. Chin, D. A. Steingart, B. P. Rand, M. C. McAlpine, *Nano Lett.* **2014**, *14*, 7017; <https://doi.org/10.1021/nl5033292>.
- [53] J. U. Lind, T. A. Busbee, A. D. Valentine, F. S. Pasqualini, H. Yuan, M. Yadid, S.-J. Park, A. Kotikian, A. P. Nesmith, P. H. Campbell, J. J. Vlassak, J. A. Lewis, K. K. Parker, *Nat. Mater.* **2016**, *16*, 303.
- [54] K. Fukuda, K. Hikichi, T. Sekine, Y. Takeda, T. Minamiki, D. Kumaki, S. Tokito, *Sci. Rep.* **2013**, *3*, 2048. <https://doi.org/10.1038/srep02048>.
- [55] D. Stauffer, A. Aharony, *Introduction to Percolation Theory*, Taylor & Francis, London, UK **1994**.

- [56] A. Sydney Gladman, E. A. Matsumoto, R. G. Nuzzo, L. Mahadevan, J. A. Lewis, *Nat. Mater.* **2016**, *15*, 413.
- [57] A. E. Jakus, E. B. Secor, A. L. Rutz, S. W. Jordan, M. C. Hersam, R. N. Shah, *ACS Nano* **2015**, *9*, 4636.
- [58] H. J. Qi, M. C. Boyce, *Mech. Mater.* **2005**, *37*, 817.
- [59] M. Amjadi, A. Pichitpajongkit, S. Lee, S. Ryu, I. Park, *ACS Nano* **2014**, *8*, 5154.
- [60] B.-U. Hwang, J.-H. Lee, T. Q. Trung, E. Roh, D.-I. Kim, S.-W. Kim, N.-E. Lee, *ACS Nano* **2015**, *9*, 8801.
- [61] J.-H. Kong, N.-S. Jang, S.-H. Kim, J.-M. Kim, *Carbon* **2014**, *77*, 199.